Mechanisms of Pore-Clogging Using a High-Resolution CFD-DEM Colloid Transport Model

Shitao Liu[1] · Igor Shikhov[1] · Christoph Arns[1]

Abstract

Colloidal transport and clogging in porous media is a phenomenon of critical importance in many branches of applied sciences and engineering. It involves multiple types of interactions that span from the sub-colloid scale (electrochemical interactions) up to the pore-scale (bridging), thus challenging the development of representative modelling. So far published simulation results of colloidal or particulate transport are based on either reduced set of forces or spatial dimensions. Here we present an approach enabling to overcome both computational and physical limitations posed by a problem of 3D colloidal transport in porous media. An adaptive octree mesh is introduced to a coupled CFD and DEM method while enabling tracking of individual colloids. Flow fields are calculated at a coarser scale throughout the domain, and at fine-scale around colloids. The approach accounts for all major interactions in such a system: elastic, electrostatic, and hydrodynamic forces acting between colloids, as well as colloids and the collector surface. The method is demonstrated for a single throat model made of four spherical segments, and the impact of clogging is reported in terms of the evolution of the critical path diameter for percolation and permeability. We identified four stages of clogging development depending on position and time of individual colloid entrapment, which in turn correlates to a cluster evolution and local transport.

Keywords Colloid transport · Pore clogging · CFD-DEM modelling · Permeability

1 Introduction

Colloidal transport and retention in porous media constitutes a major and persistent problem in hydrology and water management (Harvey and Garabedian 1991; Adin and Alon 1986), carbon sequestration (Sokama-Neuyam et al. 2017), and in a wide range of filtration applications in chemical and energy engineering (Ravikumar and Scott 2012; Lohaus et al. 2018; Tang et al. 2023). The colloid filtration theory (CFT) (Yao et al. 1971) is commonly used to describe colloid retention behaviour in saturated porous media. CFT, which

---

✉ Christoph Arns
c.arns@unsw.edu.au

[1] School of Minerals and Energy Resources Engineering, University of New South Wales, Sydney, NSW 2052, Australia

employs Happel's sphere-in-cell model (Happel 1958), treats the filtration system as an assembly of spherical grains entirely surrounded by fluid layers, thereby providing a fundamental framework for comprehending colloid retention. However, this theory does not encompass all microscopic retention mechanisms, primarily due to its lack of consideration for the locally variable geometry of the porous media.

There are three naturally different mechanisms, which may contribute to colloid retention: straining, bridging, and surface attachment. Straining occurs when pore constrictions are physically too small to allow the traverse of colloids (jamming) (Herzig et al. 1970) and is sensitive to the pore geometry. Pore space constrictions or crevices created by contacting grains are more likely to contribute to a higher probability of straining. Conversely, straining may be absent in classical collector models where spheres are not in close packing (Messina et al. 2016). Furthermore, in some realistic systems, such as rough-walled rock fractures, particles can become locally strained by getting trapped in the indentations and irregularities of a rough surface (Zhang and Prodanovic 2019). Bridging occurs when multiple colloidal particles arrive simultaneously at the pore constriction and form a stable bridge-like formation (Ramachandran and Fogler 1999). This process depends on colloid concentration, hydrodynamic conditions and a ratio of colloid to the pore throat sizes (Ramachandran et al. 2000). Colloid attachment (mechanism) refers to the retention of the colloid on a collector surface in the event of contact, typically governed by electrostatic interactions, but also including gravitational sedimentation (Yao et al. 1971). It is assumed that surface attachment is the primary mechanism of colloid retention in a porous medium when the size of the colloid is much smaller than the size of the pore throat (Kretzschmar 2005). All these three retention mechanisms may contribute to the clogging of individual pores or throats within a porous medium. While straining and bridging could cause immediate pore blockages, the electrostatic surface interactions may assist to generate multi-layered retention structures via a continual process of colloid attachment, which progressively reduces the critical flow path diameter (Katz and Thompson 1987), eventually leading to a complete pore blockage (Dersoir et al. 2015). In the progressive clogging build-up process caused by colloidal surface interactions, the fluid flow within the pore space is influenced by the growth or release of retained colloids. In turn, the behaviour of the fluid flow dictates the trajectory of incoming colloids, thereby influencing the build-up process of clogging structures.

A range of numerical approaches including Euler-Euler (Iliuta and Larachi 2006), Euler-Lagrange (Tsuji et al. 1993), fully Lagrange (Nelson and Ginn 2011), as well as statistical modelling approaches have been developed to gain a deeper insight into the pore-scale colloid transport and retention behaviour of porous media. A primary source of complexity of modelling colloidal flow in porous media is the orders of magnitude difference in characteristic length scales between collector, colloids and fluid velocity gradient. The numerical approach of coupling computational fluid dynamics with the discrete element method (CFD-DEM) is a promising way to solve these difficulties by treating the colloid phase as an individual and the fluid phase as a continuum (Cundall and Strack 1979). The CFD-DEM approach predicts colloid trajectories by calculating the resultant force acting on each particle, which includes the hydraulic forces imposed by the surrounding fluid flow. In CFD-DEM modelling, the flow domain is discretised into a mesh comprising interconnected cells that serve as the fundamental elements for calculating the fluid field and fluid-colloid interactions. The coupling between CFD and DEM can be of two types depending on whether colloid shape is resolved by the CFD mesh (Xiong et al. 2012; Hager et al. 2014) or not (Zhou et al. 2010). In the unresolved model, the mesh cell is larger than the particle size, and the fluid-particle interactions are indirectly calculated by employing a

momentum exchange term based on the particle volume fraction of the located cell. Consequently, the boundary of the particles and the velocity and pressure fields around specific particles are not resolved. While in the resolved model, the particle geometry is resolved using cells smaller than particles, and the fluid drag is calculated by integrating the interaction forces exerted by fluid over the particle surface. In the unresolved model, the lower CFD mesh resolution results in reduced computational costs, which is one of the reasons that the unresolved method is frequently employed to investigate fine particle or colloid transport and retention in porous media. Mirabolghasemi et al. (2015) employed the unresolved CFD-DEM approach to simulate the physical retention (straining and bridging) of fine particles within the sandstone. By combining the particle entrapment rate provided by the CFD-DEM simulations with the deep bed filtration (DBF) model, a porosity profile matching experiment was obtained. To save computational cost, simulations of fluid flow were not coupled with particle motion; hence, the variations of fluid pathways caused by pore-clogging phenomena were not taken into account. Lohaus et al. (2018) included the colloid-colloid and colloid-solid electrostatic surface interactions in the unresolved CFD-DEM method to investigate the clogging phenomenon during a fouling process. However, the unresolved approach falls short in capturing flow dynamics at colloid size scale, specifically important in the regions of colloid clustering, which is likely to and may severely impair simulation results. Therefore, to replicate fine-scale colloidal motions and velocity gradients critical in realistic scenarios of clogging, the resolved CFD-DEM based on a high-resolution CFD grid is desired, despite obvious implications of computational complexity.

Studies (Mondal et al. 2016; Elrahmani et al. 2022) applied a resolved CFD-DEM approach to investigate hydrodynamic bridging and the subsequent clogging phenomena for different flow rates. In these studies, the effects of colloidal surface forces on clogging are not considered, and the clogging is only governed by the hydraulic impacts and the relative size ratio between particles and pore constriction size. Kermani et al. (2020) combined the DEM and the lattice Boltzmann method (LBM) to simulate colloid transport through single pore constrictions in 2D including the electrostatic surface interactions and investigate the effects of colloid size and flow rate on colloid retention and clogging. With the consideration of colloid-colloid DLVO interactions which play a significant role in pore clogging, their model could predict colloid transport without the common assumptions, such as dilute suspension and clean bed. Nevertheless, a three-dimensional model has the potential to depict the pore clogging process in a more realistic manner. The octree mesh refinement (Popinet 2003) is an advanced meshing strategy for complex flow domains, which is capable to refine the computational mesh at the edges of the flow domain. This not only facilitates enhanced adaptability to the physical geometry of the problem but also promotes a superior representation of the flow domain's intricate boundaries. In CFD-DEM modelling, the octree mesh refinement can locally refine the mesh around the simulated particles. This effectively decreases the total number of global cells required for resolving particles and thus the computational cost (Nguyen et al. 2021).

In this study, we present a numerical approach to model colloidal particle retention and the subsequent clogging in 3D, accounting for straining at grain-grain contacts, bridging and surface attachment driven by both colloid-colloid and colloid-solid electrostatic surface interactions. An octree mesh, recursively subdividing the colloid-occupied cells to the desired resolution, is employed to greatly reduce computational cost. The evolution of the clogging process and associated reduction of hydraulic radius due to the build-up of a colloid cluster is quantified using trajectory analysis and classified into distinct stages, to our knowledge for the first time. We further show the significance of the positioning of the first

trapped colloid in the development of the clogging process for a simple, but non-trivial geometry.

2 Methodology

In this section, we introduce the CFD-DEM modelling framework, the tracking of individual colloidal particles, and observables utilised to describe the evolution of the transport parameters of the system, namely permeability and critical flow path diameter.

2.1 CFD-DEM Modelling Framework

The motion of colloids within a saturated porous medium is determined by the force balance acting on each colloid, namely collision-induced contact forces, electrostatic surface forces, and fluid drag. We simulate the trajectory of each individual colloid by using the DEM, implemented in the LIGGGHTS® software package (Kloss et al. 2012). Concurrently, the incompressible fluid flow through the given pore structure is simulated using the Finite Volume Method contained in the computational fluid dynamics package Open-FOAM® (Weller et al. 1998). To mimic the reciprocal influences of fluid flow on colloid transport and vice versa the coupling between the colloid motion and the fluid flow dynamics is implemented using the package CFDEM® (Goniva et al. 2012). Building upon the work of Liu et al. (Liu et al. 2023), who incorporated electrostatic surface interactions between colloids and collectors into the CFD-DEM modelling, this study introduces the surface interactions between colloids into the same computational framework. The trajectory of colloid i that collides either with other colloids j or/and the collector surface k is predicted by solving the translational and rotational motion equations:

$$m(i)\frac{d\mathbf{v}(i)}{dt} = \sum_{j=1}^{N} F_c^n(i,j) + \sum_{j=1}^{N} F_c^t(i,j) + \sum_{j=1}^{N} F_s(i,j) + F_c^n(i,k)$$
$$+ F_f(i,k) + F_s(i,k) + F_u(i) + F_l(i) + F_g(i); \tag{1}$$

$$\frac{dI(i)\omega(i)}{dt} = \sum_{j=1}^{N} r_{ic} \times F_c^t(i,j) + r_{ic} \times F_f(i,k), \tag{2}$$

where $\mathbf{v}$ and m are colloid velocity and mass. N is the number of colloids and self-terms $i = j$ in the sums are excluded. F_c^t is the tangential contact force due to collisions between colloids. F_c^n and F_s are the normal contact forces due to collisions and the surface forces due to electrokinetic potential. F_u, F_l and F_g are the fluid drag, buoyancy and gravity, respectively. F_f is the frictional force applied from the collector surface to oppose the colloid motion. I, ω and r_{ic} are the rotational inertia, angular velocity and torque radius, respectively.

The significance of diffusion on colloid motion can be evaluated by the Péclet number, defined as the ratio of the time required for a colloid to diffuse across a characteristic length to the time taken for the same colloid to be transported across the same distance by advection. If the Péclet number is much larger than 1, it indicates that the advection time is much shorter than the diffusion time, meaning that advection is the dominant transport and the diffusion effects can be ignored (Huysmans and Dassargues 2005). For the set of conditions and

especially due to the size of colloids considered in this work, Péclet number is much greater than 1, thus the diffusion motion is neglected.

Based on Hertz contact theory (Hertz 1882), Cundall and Strack (1979) developed the numerical scheme (also known as the soft sphere model) providing a solution for two colliding spherical particles. This "spring-dashpot" model describes the viscoelastic contact both in the normal and tangential directions, shown in Fig. 1. The spring simulates the elastic component that leads to a rebound of the colliding colloids, and the dashpot mimics the viscous component that associates the energy losses with damping mechanisms. In this work, the non-linear relationship between the contact force and the spatial overlap of two spheres is utilised following Kruggel-Emden et al. (2006)

$$F_c^n = k_n \delta_n(i,j) - \gamma_n v_n(i,j), \tag{3a}$$

$$F_c^t = \min \left\{ \left(k_t \delta_t(i,j) - \gamma_t v_t(i,j) \right), f F_c^n(i,j) \right\}, \tag{3b}$$

where k_n and k_t are the normal and tangential elastic stiffness. γ_n and γ_t are the normal and tangential damping constants. δ_n, δ_t, v_n and v_t are the normal and tangential components of the overlap distance and relative velocities, respectively. f is the friction coefficient.

The surface force $F_s(i,j)$ between the colloid i and the colloid j is evaluated by the DLVO theory (Derjaguin 1940; Verwey and Overbeek 1955) which accounts for the net potential from electrostatic repulsion and van der Waals attraction at the corresponding separation distance. The electrostatic repulsion is approximated by the screened Coulomb repulsion (Yukawa potential) (Safran 2003). The van der Waals potential between two spherical colloids is calculated following Hamaker (1937). These two surface interactions are, respectively, given by

$$U_{\text{elec}}(i,j) = \frac{2\pi r \varepsilon_0 \varepsilon_r \kappa \psi^2 e^{-\kappa(d-(r_i+r_j))}}{\kappa}, \tag{4}$$
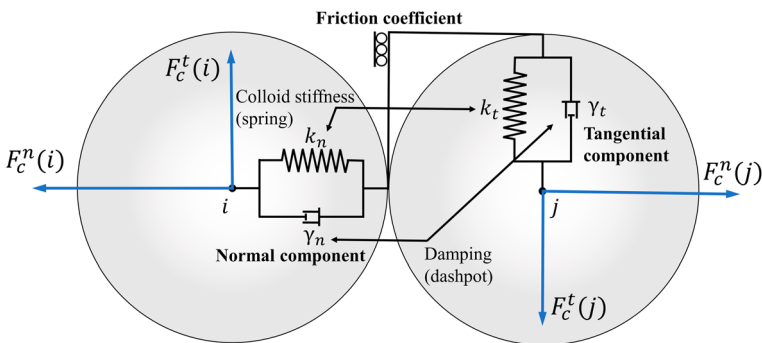

Fig. 1 Schematic of the spring-dashpot mode mimicking forces acting on two spheres during elastic collision

$$U_{\text{van}}(i,j) = -\frac{A}{6}\left[\frac{2r_ir_j}{d^2 - (r_i + r_j)^2} + \frac{2r_ir_j}{d^2 - (r_i - r_j)^2}\right.$$
$$\left. + \ln\left(\frac{d^2 - (r_i + r_j)^2}{d^2 - (r_i - r_j)^2}\right)\right], \quad (5)$$

where r_i, r_j and d are the radius of colloid i, the radius of colloid j, and the distance between the centers of two interacting colloids, respectively. ε_0 is the dielectric permittivity of vacuum ($8.854 \times 10^{-12}\,CV^{-1}\,m^{-1}$) and ε_r is the relative dielectric permittivity of solution, here water (78.55 at $298\,K$). ψ is the colloid surface potential. A is the Hamaker constant which is mainly controlled by the dielectric properties of colloids and the carrier fluid. κ is the inverse Debye length representing the physical scale of the near surface electrical double layer

$$\kappa = \sqrt{\frac{2e^2N_AI_s}{\varepsilon_r\varepsilon_0k_bT}}, \quad (6)$$

where e, N_A and I_s are the elementary charge ($1.602 \times 10^{-19}\,C$), Avogadro constant ($6.02 \times 10^{23}\,mol^{-1}$) and the ionic strength of the solution, respectively.

The surface force between the colloid i and the collector surface k is modelled following the DLVO theory for the sphere-plate system (Huang et al. 2018). The DVLO potential combines three interactions: the electrostatic double layer, van der Waals and the Born repulsion, quantified following (Hogg et al. 1966), Gregory (1981) and Ruckenstein and Prieve (1976), respectively:

$$U_{elec}(i,k) = \pi\varepsilon_r\varepsilon_0r_i\left\{2\psi_i\psi_k\ln\left[\frac{1 + e^{(-\kappa d)}}{1 - e^{(-\kappa d)}}\right]\right.$$
$$\left. + \left(\psi_i^2 + \psi_k^2\right)\ln\left[1 - e^{(-2\kappa d)}\right]\right\}, \quad (7)$$

$$U_{van}(i,k) = -\frac{A}{6}\left[\frac{2r_i(d + r_i)}{d(d + 2r_i)} - \ln\left(\frac{d + 2r_i}{d}\right)\right], \quad (8)$$

$$U_{br}(i,k) = \frac{A\delta_{br}}{7560}\left[\frac{8r_i + d}{(2r_i + d)^7} + \frac{6r_i - d}{d^7}\right], \quad (9)$$

where the Born collision parameter is chosen as $\delta_{br} = 0.5\,nm$ (Israelachvili 2011). A typical DLVO potential as a function of separation distance between the colloid and the collector's surface can be qualitatively characterised as having three distinct regions: weak net attraction at long distance, having a shallow (secondary) minimum; very strong attraction at short distance (primary minimum) and a local maximum in between, which may or may not act as an energy barrier preventing colloids from reaching a primary minimum state. In conditions of high ionic strength, the electrostatic double layer of ions around colloids is compressed, which screens the double layer interaction, leading to the dominance of van der Waals interactions, thus leading to the absence of an energy barrier. These conditions are favourable for colloid attachment via the strongly attractive energy at the primary minimum. To replicate conditions that favour clogging for a water-polystyrene-glass filtration system, an ionic strength of 300 mM is employed (Tufenkji and Elimelech 2005). Since the

effect of the DVLO potential does not manifest beyond the approximately 10 nm distance from the colloid surface (three orders of magnitude smaller than the colloid size), here it is neglected unless colloid-collector or colloid-colloid contact occurs.

Consider now the interaction of the colloids with the carrier fluid. The coupling between the colloid and fluid phases is achieved using a fictitious domain method (Shirgaonkar et al. 2009), which assumes that the colloid-populated regions are filled by a fictitious fluid. The hydraulic force exerted by the surrounding fluid is calculated by integrating the pressure and viscous forces acting on the colloid's surface. Firstly, the velocity and pressure field of the fluid are obtained by solving the incompressible Navier–Stokes equations on the entire flow domain Ω, consisting of colloid-populated regions Ω_s and fluid-populated regions Ω_f ($\Omega = \Omega_s + \Omega_f$). The momentum and continuity equations are expressed as

$$\frac{\partial(\rho\mathbf{u})}{\partial t} + \rho\mathbf{u}\cdot\nabla\mathbf{u} = -\nabla p + \mu\nabla^2\mathbf{u} \quad \text{in } \Omega,$$ (10)

$$\nabla \cdot \mathbf{u} = 0 \quad \text{in } \Omega,$$ (11)

where p, $\mathbf{u}$, μ and ρ are the pressure, fluid velocity, fluid viscosity and fluid density, respectively. The initial conditions and the conditions on the flow domain boundary $\partial\Omega$ are provided as:

$$\mathbf{u}(\mathbf{x}, t = 0) = \mathbf{u}_0(\mathbf{x}) \quad \text{in } \Omega,$$ (12)

$$\mathbf{u} = \mathbf{u}_{\partial\Omega} \quad \text{on } \partial\Omega.$$ (13)

After the flow field is calculated, the effects of colloid movement on fluid flow are incorporated by correcting the fluid velocity on the colloid-fluid interface $\partial\Omega_s$ to the velocity of the corresponding colloid, which is expressed as:

$$\mathbf{u} = \mathbf{u}_i \quad and \quad \sigma \cdot \hat{\mathbf{n}} = \mathbf{t}_{\partial\Omega_s} \quad on\ \partial\Omega_s,$$ (14)

where σ is the stress tensor in the fluid phase. $\hat{\mathbf{n}}$ is the outward normal vector of the colloid phase and $\mathbf{t}_{\partial\Omega_s}$ is the traction vector acting on the surface of the colloid $\partial\Omega_s$ from the flow of surrounding fluid. Equation (14) prescribes a non-slip boundary condition on the surface of the colloid. Therefore, the fluid drag acting on the colloid i is calculated by integrating the pressure and viscous forces over the colloid-fluid interface:

$$F_u(i) = \int_{\partial\Omega_s^i} \sigma \cdot \hat{\mathbf{n}}\, d\partial\Omega_s^i = \int_{\Omega_s^i} -\nabla p + \mu\rho\nabla^2\mathbf{u}\, d\Omega_s^i$$
$$= \sum_{c\in\Omega_s^i} \left(-\nabla p + \mu\rho\nabla^2\mathbf{u}\right)_c V_c,$$ (15)

where V_c is the cell volume, and c denotes the CFD cell.

2.2 Colloid Tracking Model

Here we consider simulation of a clogging process in a pore-throat structure constructed by four spherical segments (see Fig. 2a). This geometry generally mimics major elements of pore structures made of glass beads or rounded grains of sand, having significant
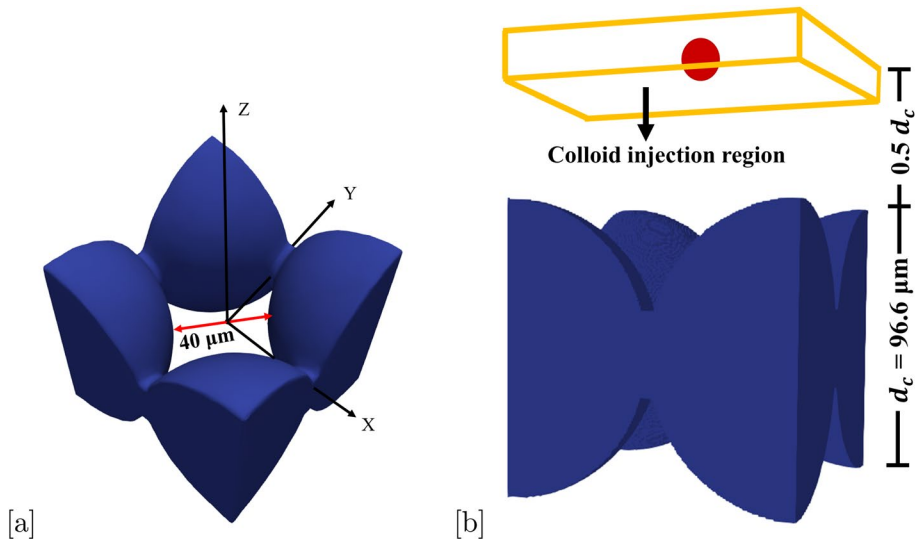
Fig. 2 The top view (**a**) and side view (**b**) of the pore constriction geometry used in colloid tracking simulations

variability of cross-sectional flow. The geometrical input for coupled CDF-DEM simulations is created in two major steps: firstly, a fine scale solid-void labelled regular grid geometry provides an accurate reference of the collector surface; secondly, that geometry is superimposed on a coarse grid of the flow domain and the surface of the collectors is constructed at intermediate resolution following a refinement process of the cells sharing void and solid labels. The diameter of the spherical collectors is $d_c = 96.6\ \mu m$, creating a throat of 40 μm in diameter (the shortest length scale), similar to the median throat size (d_{50}) of Bentheimer sandstone of 37.5 μm (Shikhov et al. 2017). The structure is discretised using a regular Cartesian grid, resulting in a voxel size of 0.48 $\mu m/vox$. The colloid suspension outflow region is placed 0.5 d_c above the collector (Fig. 2b).

To save on computational cost the flow domain grid size is 5 times the size of the original resolution of the digitised structure (2.6 μm). The generation of the CFD mesh begins by encompassing the space of both the pore and collector phases with a background cubic mesh which defines the main resolution of the fluid calculation mesh, shown in Fig. 3a. The interface between the pore phase and the collector phase in the 3D throat is overlaid on the background cubic mesh to identify cells associated with the pore phase and those corresponding to the collector phase. The next step is the splitting of the cells located at the pore-collector interface shown in Fig. 3b. Finally, all dispensable cells located within the collector phase region are discarded (Fig. 3c). The remaining cells representing the fluid domain constitute the CFD mesh for the fluid dynamics calculation. This mesh is created using the CFD mesh generation tool SnappyHexMesh.

In the resolved CFD-DEM approach, the colloid-fluid interaction force is calculated by integrating the viscous forces over the colloid surface (Eq. 15), which requires a high-resolution CFD mesh with at least eight cells per colloid diameter to resolve the colloid (Hager et al. 2014). In the following an octree mesh (Meagher 1980) is employed to achieve this resolution. Computational cost is reduced through adaptive refinement by recursively subdividing the colloid-populated cells into eight sub-cells
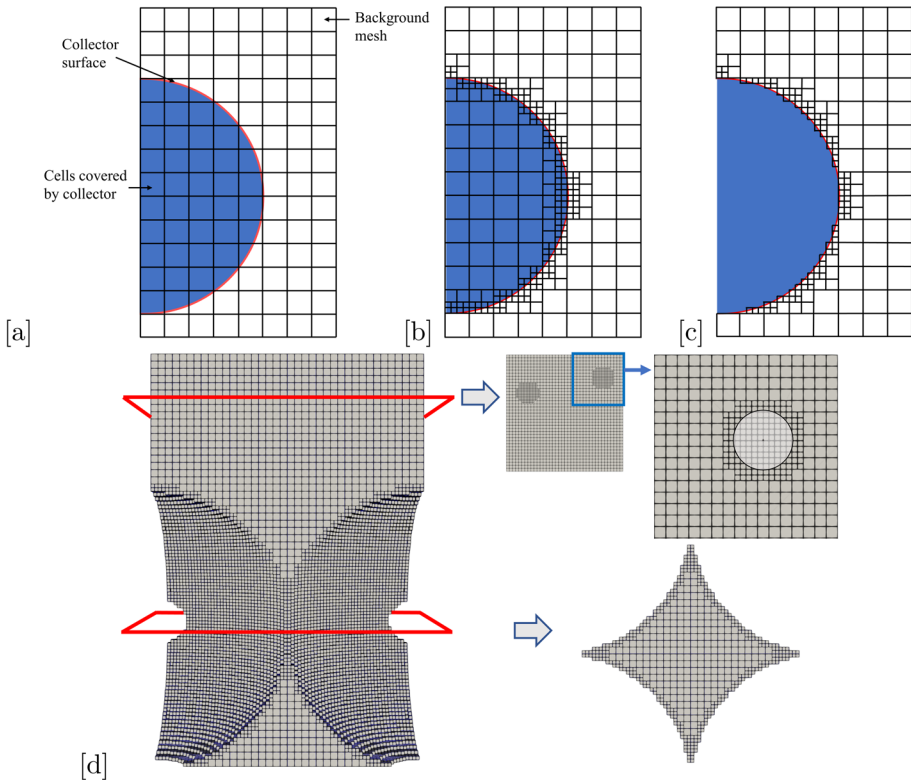
Fig. 3 Illustration of the CFD mesh generation process (**a–c**) and mesh refinement. (**a**) Background mesh, (**b**) subdivision of the cubic cells populated by the collector surface, (**c**) removal of cells located within the solid phase region. (**d**) A schematic demonstrating the generated fluid mesh and the adaptive mesh refinement of the colloid-populated region

until newly produced cells are smaller than one-tenth of the colloid diameter (shown as the upper red frame of Fig. 3d). Given the initial fluid mesh cell size of 2.6 µm and the colloid size of 13.3 µm, a one-level mesh refinement strategy, which subdivides each particle-populated cell into eight sub-cells, is adopted. This approach locally enhances the mesh resolution to 1.3 µm, ensuring that there are more than eight cells across each colloid diameter to meet the required precision. The adaptive refinement achieves a locally high resolution for colloid-fluid coupling calculations, reducing the computational cost by significantly decreasing the number of cells required in the fluid mesh. For instance, to obtain a mesh resolution of 1.3 µm, the number of cells in the fluid mesh utilising adaptive refinement is 79,532, in contrast to 538,865 cells when adaptive refinement is not used. The partitioned cells recover as soon as colloids leave. To ensure this employed mesh is sufficiently fine to provide a reliable fluid velocity calculation, we compare the calculated fluid velocity distribution on the throat cross-section derived with the employed mesh (Fig. 4a) and a mesh that is five times denser. In the fluid calculations, no-slip boundary conditions are imposed at the solid sphere surface and the outer bounding surface, and constant inlet velocity and outlet pressure boundary conditions are employed. Figure 4b shows an excellent match of the velocity distributions
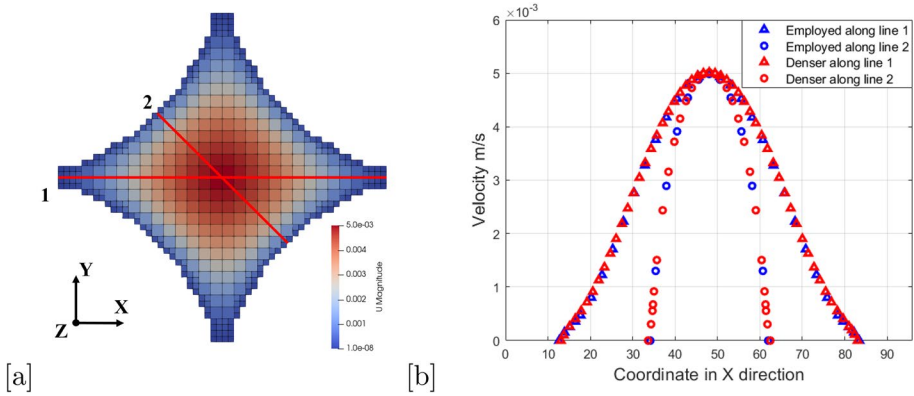
Fig. 4 The comparison of fluid velocity calculations derived from the employed mesh and a five times denser mesh. (**a**) is the fluid velocity distribution at the throat cross-section calculated by the employed mesh. (**b**) presents the profiles of fluid velocity distribution calculated by the employed and a denser mesh. The velocity distributions are investigated between two opposite grain-to-grain contacts and along the critical diameter, shown as the red line 1 and 2 in (**a**)

between these two meshes, indicating that the resolution of the employed mesh is sufficient to provide reliable fluid calculations.

Simulations are performed mimicking the pore clogging phenomenon of polystyrene latex particles of 13.3 μm with a density of $1.05\,g/cm^3$, achieving a throat-to-colloid size ratio of 3. An ionic strength of $300\,mM$ is employed, which leads to a favourable condition for colloid surface attachment. ζ-potentials of $-27.9\,mV$ and $-15.7\,mV$ are, respectively, imposed on colloid and collector surface following the measurements from Tufenkji and Elimelech (2005) to calculate the DLVO forces with a Hamaker constant for a water-polystyrene-glass system $1 \times 10^{-20}\,J$ (Li et al. 2005). For the colloid-collector DLVO interactions, a potential of $-3042\,k_b T$ corresponding to the primary minimum is utilised to introduce the interactions after colloids collide with the solid surface. In the simulations, colloids are injected at an initial velocity of $0.0005\,m/s$ and a volumetric concentration of 0.5%.

The restitution coefficient used to evaluate the energy loss during colloid-solid collision is selected following Lun et al. (1984) while the friction factor is chosen according to Ke and Gu (1998). The DEM time step is limited by a critical value of 20 percent of Rayleigh critical time (Li et al. 2005), which is capable to capture colloid-surface collision events and fulfills the requirement for numerical stability. The CFD time step is chosen based on the Courant number calculated as

$$C_0 = \frac{\mathbf{u}_f \Delta t_{\text{CFD}}}{\Delta X}, \tag{16}$$

where Δt_{CFD} and ΔX are fluid time step and cell size. The CFD time step is chosen to ensure that the Courant number does not exceed 0.5, which means that the fluid does not travel a distance longer than half the length of the control cell. The duration for information interchange between the fluid and colloid phase, noted as the coupling interval, is selected to be equivalent to the CFD time step. The final set of mechanical properties and parameters used in the simulations is summarised in Table 1.

Table 1 Parameters used in the colloid transport simulations

	Value	Unit		Value	Unit
Solid phase			*Liquid phase*		
Collector diameter	96.6	μm	Liquid density	1000	kg/m^3
Colloid diameter	13.3	μm	Liquid viscosity	1×10^{-3}	$Pa \cdot s$
Colloid density	1050	kg/m³	*Simulation time step*		
Restitution coefficient	0.9	–	DEM time step	5×10^{-8}	s
Collector Young's modulus	20	GPa	CFD time step	2×10^{-6}	s
Colloid Young's modulus	70	MPa	Coupling interval	2×10^{-6}	s
Collector Poisson's ratio	0.3	–			
Colloid Poisson's ratio	0.3	–			
Friction factor	0.15	–			

2.3 Permeability and Critical Path Diameter

Colloid suspension flow through the structure given in Fig. 2a under favourable conditions for colloid attachment is likely to lead to the build-up of a monolayer film and/ or clusters restricting the flow. We use two quantities—permeability and critical diameter (l_c), to quantify this evolution. For this analysis, the union of the original structure and all retained colloids form the micro-structure of interest. The retained colloids are added to the regular cubic grid by utilising their diameter and centre positions at given time steps and the system is discretised on a regular cubic grid with resolution of $\epsilon = 0.005d_c = 0.048 \, \mu$m (approximately 1/27 of the colloid diameter).

Given that we calculate l_c on a regular grid, we found it convenient to calculate permeability via the lattice Boltzmann method using the same discretisation utilising the D3Q19 lattice (3-dimensional lattice with 19 possible velocity directions) (Martys and Hagedorn 2002). No-slip boundary conditions are applied at the fluid-solid surface by the bounce-back rule. Periodic boundary conditions are applied in z-direction, while side boundaries are closed to flow. A small body force is applied to drive the flow (laminar flow regime).

The critical flow path diameter $l_c(t)$ defined as the diameter of the largest sphere that could percolate the porous medium is used to monitor the evolution of the opening of the pore constriction and identify the moment of clogging occurrence. Clogging is considered to occur when $l_c(t)$ becomes smaller than the colloid diameter, which means no colloid can traverse (assuming that colloids are rigid). We refer to the time at which this threshold is reached as the critical clogging time t_c. To calculate $l_c(t)$ at specific times the Euclidean distance map is calculated on the pore space. Based on the distance map, a bisection algorithm is employed to identify the diameter of the largest sphere capable of percolating through the pore-throat structure (Arns et al. 2005).

3 Results

The results section is divided into three parts. We start with describing the average evolution of the clogging process, observed over 100 independent realisations. This is followed by analysing the mechanistic details leading to the wide distribution in measured clogging times. For the latter, we select simulations where the reduction of l_c as a function of time differs significantly. We then consider in more detail how the position of first attachment of a colloid on the collector surface impacts the reduction of l_c and the critical clogging time.

3.1 Stochastic Nature of Clogging

Colloid capture and retention eventually leads to the development of colloid clusters, inducing pore clogging at the throat, and consequential reduction of critical flow path diameter and permeability. With the simulated colloid trajectories, the pore clogging process and the evolution of the critical diameter and permeability are monitored over the entire clogging process. Given the applied throat-to-colloid size ratio of three, a single layer of colloids retained on the collector surface is unlikely to obstruct colloid traversal. Pore clogging arises only after the establishment of multilayer retention enhanced by colloid-colloid interactions. In case of the dilute limit of colloidal suspension, pore clogging is a highly stochastic process. Although the same retention mechanisms are at play under identical filtration conditions, the time at which the first colloid is retained, the development progress of the first layer retention and multilayer retention, and the time required to build an impassable cluster of colloids can be different. To evaluate the stochastic nature of cluster development during the clogging process, we conduct 100 simulations with randomly changed initial positions of colloids entering the system and report standard deviation and 95% confidence interval of l_c and permeability as a function of time (see Fig. 5). Colloid tracking simulations are undertaken on the gadi supercomputer of the National Computational Infrastructure (NCI) of Australia. For each simulation, 96 processors are employed in parallel running to simulate the pore clogging process for 5 s. Approximately 3500 service units are consumed, defined as the number of processors multiplied by the run time in hours.
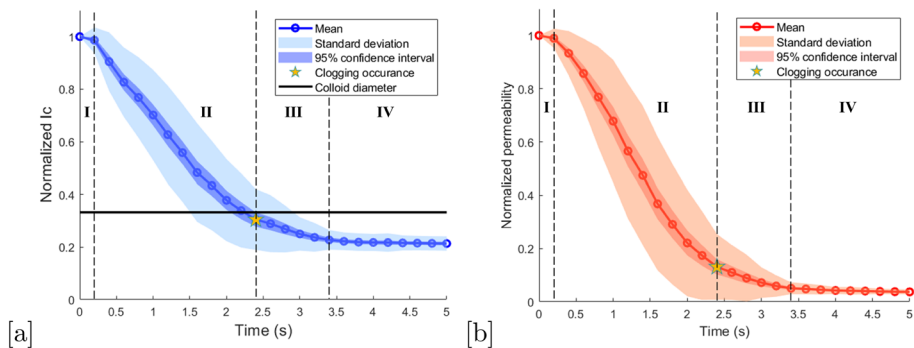

Fig. 5 Evolution of the clogging process in terms of transport properties averaged over 100 simulations: (**a**) normalised critical diameter, and (**b**) normalised permeability. The star corresponds to the average reduction in the constriction diameter, where no colloid can physically traverse (size exclusion) for the first time

The results indicate a consistent four-stage decline profile for both l_c and permeability. The first stage is characterised by a slight reduction in l_c and permeability. The relatively small standard deviation suggests that in most realisations colloid attachment has not yet occurred. We refer to the time of first colloid retainment in the system as t_1. The second stage, spanning from the beginning of filtration to the occurrence of pore clogging, is characterised by a sharp decrease in l_c and permeability. At the start, the pore-throat structure is fully open, and any particle that attaches on the collector surface near the narrowest point at this stage blocks a significant portion of the open flow path. Each individual retained colloid can lead to a significant reduction of l_c and permeability, thereby leading to a rapid decrease in both values. Subsequently, in the third stage, both l_c and permeability exhibit a slower rate of decrease. This phase concludes when the standard deviation starts to stabilise after experiencing a notable decrease, marking the start of the fourth phase.

After clogging occurs, an impassable cluster divides the throat into multiple narrower pathways which are present either between colloids or between a colloid and the collector. These pathways grow in length and are randomly narrowed further by newly retained colloids. Eventually, the cluster starts to evolve into a structure resembling a random close packing of spheres, where the constrictions along fluid pathways are mainly controlled by the size of the pores between the retained colloids within the cluster. Given the colloidal system is monodisperse, the pore size distribution of the cluster is expected to remain narrow during cluster growth and across different realisations, which is reflected by a slow decline of l_c and permeability during the fourth stage. This "pseudo bead pack" behaviour of colloidal cluster also results in a sharp decrease of standard deviation of l_c and permeability, which separates the third the fourth stages. In the long term limit, the minimum value of l_c is limited by the critical diameter of a pore constriction located on the lateral flat boundary of the flow domain. The constriction is formed by colloids that touch tangentially, in conjunction with the lateral flat boundary of the flow domain. This critical diameter is equivalent to 0.25 times the colloid diameter (13.3 µm) (Roozbahani et al. 2014). The mean of simulated l_c at the end of simulations is 8.4 µm, i.e. significantly larger than the limiting value. This discrepancy arises because the considered system (given the chosen colloids and pore system sizes) does not allow to accommodate a sufficient number of colloids to form an uncorrelated random close packing of spheres. Permeability decreases by a factor of 25 compared to its initial value, indicating that the clogging structure significantly impairs the throat's flow capacity.

3.2 Analysis of Individual Cases

Two realisations of pore clogging (named *R1* and *R2*), in which the reduction of the critical path diameter and permeability as a function of time are significantly different are chosen to illustrate the mechanistic details of the formation of an impassable cluster at the throat. The pore clogging build-up processes of the two chosen realisations are illustrated in Fig. 6.

Figure 6a demonstrates a four-stage temporal evolution of l_c for *R1* including corresponding retained colloid configurations at specific time steps. In the beginning, colloids traverse the throat without attaching the collector, associating the first stage. The second stage, noticeable by a significant l_c reduction, spans from the onset of individual colloid retention to the occurrence of pore clogging. Soon after the beginning of the colloid suspension inflow, one of the colloids is intercepted by the collector surface and retained by strong attractive DLVO forces. Due to the combination of hydrodynamic drag and
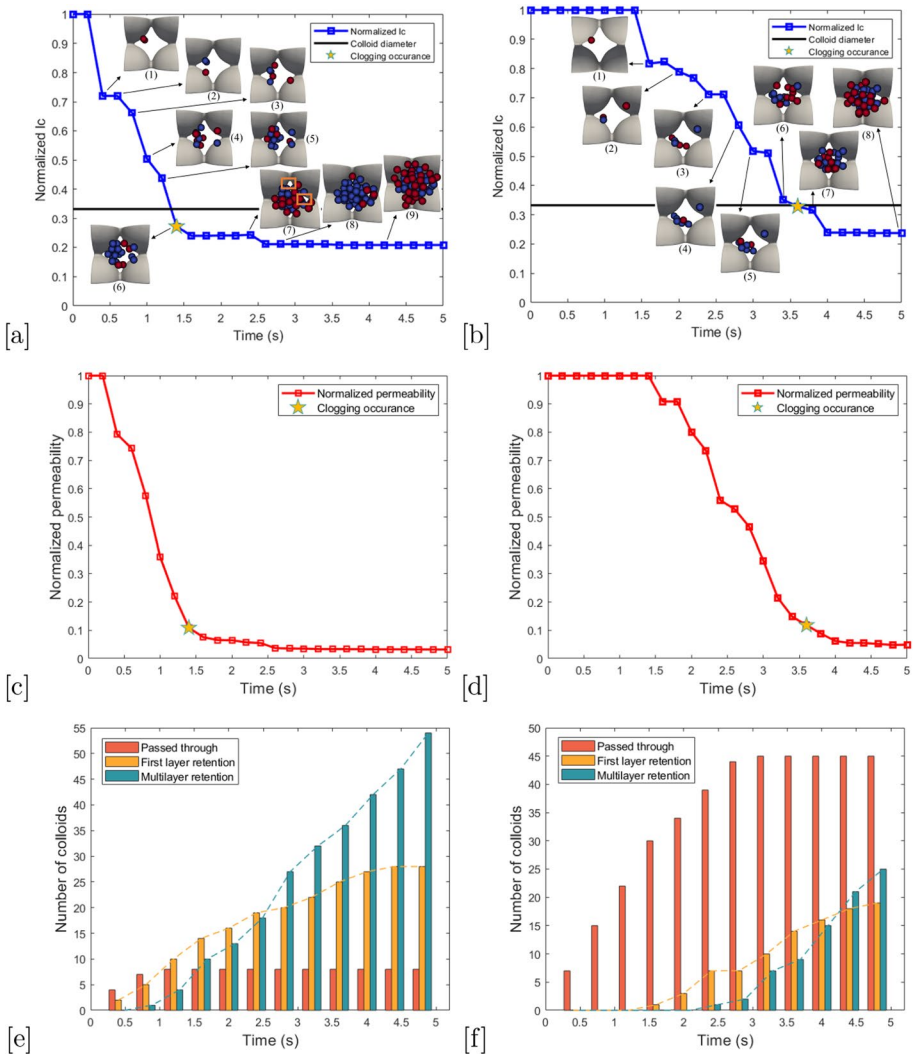
Fig. 6 Two chosen realisations of pore clogging process with distinct colloid insertions, *R1* (left) and *R2* (right). (**a**) Evolution of the critical flow path diameter l_c of the *R1*. (**b**) Evolution of the critical flow path diameter l_c of the *R2*. The instantaneous configurations of retained colloids are shown at their corresponding simulation times. The red colloids represent the freshly retained colloid since the last shown colloid configuration. (**c**) Evolution of permeability of the *R1*. (**d**) Evolution of permeability of the *R2*. (**e**) Changes in the number of traversed colloids, the number of colloids in the first layer retention and multilayer retention of the *R1*. (**f**) Changes in the number of traversed colloids, the number of colloids in the first layer retention and multilayer retention of the *R2*. In (**a**–**d**) l_c and permeability are normalised by their initial values when no colloid is retained in the system

inter-colloidal surface force, the incoming colloid rolls along the surface of the attached colloid, moving downstream until it is captured by the collector surface (Fig. 6a, configuration (1)). The position of the second attached colloid is closer to the centre of the throat and effectively decreases l_c by nearly one-third. The forming aggregate of colloids grows

from the pore entrance to the throat along the flow direction due to the rolling on the previously deposited colloids, which results in a more significant reduction of l_c. The aggregate not only spreads on the grain surface as the first layer, held by colloid-collector interactions, but also grows towards the pore centre as a second and subsequent layers of colloids are retained due to colloid-colloid interactions (Fig. 6a, configurations (3–5)).

At the same time, colloids are successively captured on the opposite side of the throat entry forming a second aggregate. Upon increase in size, both aggregates eventually merge (Fig. 6a, configuration (6)). This merger further decreases l_c to a size less than the diameter of the colloid, indicating that no additional colloids can traverse the throat, which leads to pore clogging. In this period, the flow path through the pore progressively narrows and eventually splits into several narrower flow paths because of retained colloid aggregates. Once the throat is clogged, all injected colloids are captured at the front of the growing cluster (Fig. 5a, configuration (6–8)). This accumulation of colloids results in a further decrease in l_c but at a substantially slower rate, as the divided flow paths are progressively narrowed or blocked. For instance, the two pore openings, indicated by the orange rectangles in Fig. 6a, configuration (7), become closed in configuration (8). This progression marks the third stage. Finally, since most paths are closed by retained colloids, the further accumulation of retained colloids has almost no contribution to the l_c reduction, marking the fourth stage of this process.

The retained colloids effectively narrow the flow pathway and increase the hydrodynamic resistance, which decreases the permeability of the pore-throat structure. Figure 6c demonstrates the evolution of the permeability during the clogging progress, which shows a trend similar to the evolution of l_c decreasing in four stages. This similarity indicates a strong correlation between permeability and l_c, as previously observed (Katz and Thompson 1987; Arns et al. 2005). A minute difference between permeability and l_c trends is due to different impact of colloids located far away from the throat, which do not decrease l_c but do reduce permeability. One such example is the transition from configuration (1) to configuration (2) in Fig. 6a and c: while l_c is constant, the permeability decreases since this retained colloid reduces the available pore space for fluid flow and increases the hydrodynamic resistance. Overall, the individual retained colloids lead to a significant reduction of l_c and permeability during the second stage. In the third and the fourth stages, even though all incoming colloids are retained, the impact on l_c and permeability is less important.

The temporal evolution of l_c and permeability of *R2* are shown in Fig. 6b and d, respectively. Figure 6b shows a similar progression of the pore clogging built-up process compared to *R1*, including single colloid capture, colloid cluster development (the first layer and multilayer retention), and the merger of colloid clusters. However, both l_c and permeability of *R2* demonstrate a delayed reduction compared to *R1*. There is a relatively long inactivity period at the beginning of the injection, during which no colloid is intercepted by the collector surface (Fig. 6b, configuration (1); first capture after $\approx$ 1.5s).

An alternate representation of clogging dynamics is the grouping of colloids into three populations as a function of time: those which traversed the pore-throat structure, those retained in the first layer, and colloids retained in the second and subsequent layers (Fig. 6e, f). Before clogging of the throat, the first layer retention develops at a higher rate than multilayer retention. Once a stable clogging structure is established, the only retention mechanism is multilayer retention (Fig. 6e, f). The main difference between cases *R1* and *R2* is the number of traversing colloids before the first one is captured and the impact on l_c from the first several colloids attached. Another interesting observation is that colloidal clusters in both cases become practically impassible (no traversing colloid) well before a clogging event when l_c becomes smaller than colloid diameter. Clearly, when the opening within the

cluster only slightly exceeds the colloid size, the probability for the very next colloid to be captured and thus triggering full clogging is almost certain.

3.3 Initial Phase of Colloid Cluster Assembly

The time and position at which the first few colloids are captured on the collector surface may govern the clogging process. One relationship we investigate is between the retention position of the first captured colloid and the clogging critical time. We use the angle α between the colloid attachment location and the throat to quantitatively express the proximity of the retained position to the narrowest cross-section to flow, while time is counted starting from the capture of the first colloid $(t_c - t_1)$, Fig. 7a.

Figure 7b demonstrates the distribution of clogging build-up time as a function of α for the 100 tracking simulations, where data is fitted with a linear function utilising a linear least squares regression. The proximity of the first captured colloid to the throat constriction (smaller α values) expectedly leads to faster clogging due to a more significant l_c reduction (Fig. 7b). However, these "clogging starter" colloids are relatively rare, since the "sweet spot" range of α projected onto the injection region corresponds to a small area and thus very small fraction out of all colloids. Although, the position of the first colloid does not uniquely define critical clogging time, since quite significant spread in time for a given α is observed. This variability is primarily due to the stochastic nature of the clogging process, which is significantly affected by the subsequent development of a colloid cluster.

The injection position of colloids defines their trajectories and retention behaviour. On one hand, the variation in fluid velocities at different injection positions leads to diverse hydrodynamic forces acting on the colloids, which influences the subsequent motion of colloids. On the other hand, the distance between the streamline associated with insertion position and the collector surface defines the probability of colloid intersection. The colloids or clusters retained within the throat can serve as additional collectors, enhancing the capture of incoming colloids.
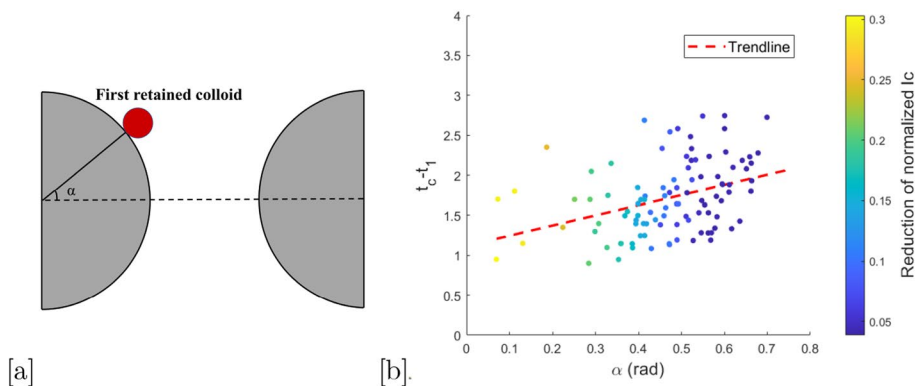

Fig. 7 (**a**) A schematic demonstrating the angle α representing the proximity of the retained position to the narrowest point. (**b**) The clogging critical time $(t_c - t_1)$ distribution as a function of α. The color bar represents the l_c reduction caused by the first retained colloid in each simulation. The trendline indicating the trend of clogging build-up time as a function of α is generated by fitting these data points with a linear least squares regression
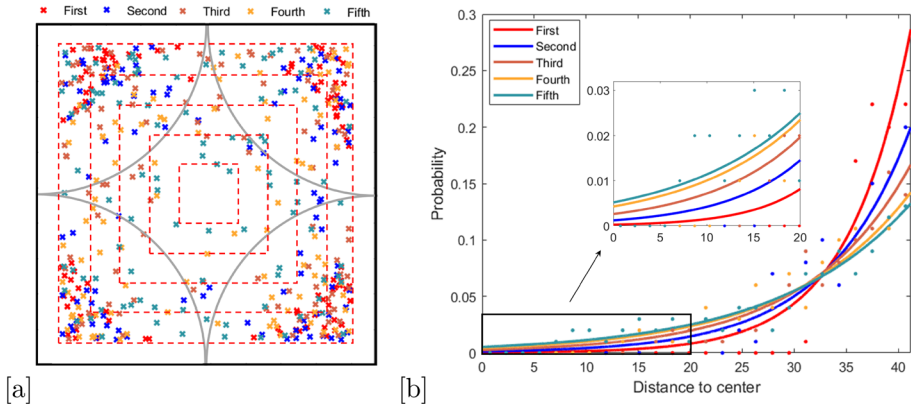
Fig. 8 The spatial distribution of the injection positions of the first five retained colloids from 100 independent simulations. (**a**) A top view slice of colloid injection domain (perpendicular to the flow direction) divided into square segments with 3 μm width step. The colored points represent the projection of the injection positions of the first five retained colloids. (**b**) The probability distribution of injection positions of the first five retained colloids

We divide the colloid injection region slice (perpendicular to the flow direction) by a series of concentric squares with parallel sides, Fig. 8a to illustrate the injection positions of the first five retained colloids in each of 100 simulations. This representation reveals a progressive change of the injection position from the collectors uppermost parts (first to third captured colloids) towards the inner throat region (fourth and especially fifth captured colloid), thus setting the stage for cluster development at the throat. For such colloids that are injected above the collector center, the distance between the located streamline and the grain surface diminishes to less than the colloid radius as the streamline deforms and converges towards the pore center at the constriction. While the colloids that are injected above the throat projection traverse the throat without obstruction. Due to the attractive colloid-colloid surface interactions, the retained colloids act as additional collectors to capture the subsequently incoming colloids. As the clusters expand towards the pore center through the formation of multilayer retention structures, incoming colloids can be retained even when they are introduced near the pore center. Compared with the first retained colloid, the injection positions of the fifth retained colloid exhibit a more widespread distribution that almost covered the entire slice area.

Figure 8b displays the probability distribution of injected positions for the first five retained colloids within the series of square annuli, as well as the fitting curves obtained using the exponential function, with corresponding R-squared values ranging from 0.89 to 0.94. Colloids that are injected at a greater distance from the pore center exhibit a higher probability of being retained. From the first to the fifth retained colloid, the proportions of injection positions located at greater distances to the pore center (40 μm) progressively diminish. In contrast, a higher proportion of injection positions close to the pore center is observed for the colloid retained later in the sequence. This indicates that as more colloids are retained, the constraint on injection positions resulting in retention is gradually relaxed, allowing for a broader range of colloid injection positions to lead to retention.

4 Conclusion

This study proposed a resolved CFD-DEM model to mimic the pore clogging process within a single converging–diverging pore structure, including the electrostatic surface interactions and hydrodynamic effects on the microscopic scale. We employ an octree mesh technique, which adaptively refines the colloid-populated cells to the desired resolution, effectively decreasing the overall number of CFD cells and reducing the computational cost. The critical diameter l_c and LBM-calculated permeability are employed to monitor the evolution of transport properties over the entire clogging process. The individual simulations show that clogging is a highly stochastic process governed by the retained cluster configurations and their subsequent growth. The mean of 100 simulations demonstrates a consistent shape of l_c and permeability evolution profiles, which indicates l_c is a length scale strongly related to permeability. l_c and permeability decrease as a function of time in four stages during the clogging process: (1) constant prior to any colloid capture; (2) fast reduction at nearly constant rate before clogging; (3) modest reduction with limited colloid retention after clogging; (4) minor reduction with the subsequent pile-up of colloids. Subsequently, we examine the impact of initial colloid retention on the development of clogging and find that a closer first colloid capture to the throat tends to accelerate the clogging process. Finally, we investigate the distributions of the injection position of retained colloids in sequence and find that the injection potions that potentially result in retention are expanded from the projection of the collector phase projection to the throat center as an increasing number of colloids are retained in the system.

In the pore-throat filtration system utilised in this study, no definite detachment and reattachment are observed. This is attributed to the strong attractive surface interactions under favourable conditions and the limited size of the flow domain. In future work we will consider larger and more realistic systems like rocks, represented by micro-CT images, exhibiting a more complex pore geometry and surface roughness. It is expected that the modelling approach presented here is efficient enough for such calculations and can provide additional insights of colloid transport and retention which may lead to improved analytical expressions.

Declarations

Conflict of interest The author declare that they have no conflict of interest.

References

Adin, A., Alon, G.: Mechanisms and process parameters of filter screens. J. Irrig. Drain. Eng. **112**(4), 293–304 (1986). https://doi.org/10.1061/(ASCE)0733-9437(1986)112:4(293)

Arns, C.H., Knackstedt, M.A., Martys, N.S.: Cross-property correlations and permeability estimation in sandstone. Phys. Rev. E **72**, 046304 (2005). https://doi.org/10.1103/PhysRevE.72.046304

Cundall, P.A., Strack, O.D.L.: A discrete numerical model for granular assemblies. Géotechnique **29**(1), 47–65 (1979). https://doi.org/10.1680/geot.1979.29.1.47

Derjaguin, B.: On the repulsive forces between charged colloid particles and on the theory of slow coagulation and stability of lyophobe sols. Trans. Faraday Soc. **35**, 203–215 (1940). https://doi.org/10.1039/TF9403500203

Dersoir, B., de Saint Vincent, M.R., Abkarian, M., Tabuteau, H.: Clogging of a single pore by colloidal particles. Microfluid. Nanofluidics. **19**, 953–961 (2015). https://doi.org/10.1007/s10404-015-1624-y

Elrahmani, A., Al-Raoush, R.I., Abugazia, H., Seers, T.: Pore-scale simulation of fine particles migration in porous media using coupled CFD-DEM. Powder Technol. **398**, 117130 (2022). https://doi.org/10.1016/j.powtec.2022.117130

Goniva, C., Kloss, C., Deen, N.G., Kuipers, J.A., Pirker, S.: Influence of rolling friction on single spout fluidized bed simulation. Particuology **10**(5), 582–591 (2012). https://doi.org/10.1016/j.partic.2012.05.002

Gregory, J.: Approximate expressions for retarded van der Waals interaction. J. Colloid Interface Sci. **83**(1), 138–145 (1981). https://doi.org/10.1016/0021-9797(81)90018-7

Hager, A., Kloss, C., Pirker, S., Goniva, C.: Parallel resolved open source CFD-DEM: method, validation and application. J. Comput. Multiph. Flows. **6**(1), 13–27 (2014). https://doi.org/10.1260/1757-482X.6.1.13

Hamaker, H.C.: The London-van der Waals attraction between spherical particles. Physica **4**(10), 1058–1072 (1937). https://doi.org/10.1016/S0031-8914(37)80203-7

Happel, J.: Viscous flow in multiparticle systems: slow motion of fluids relative to beds of spherical particles. AIChE J. **4**(2), 197–201 (1958). https://doi.org/10.1002/aic.690040214

Harvey, R.W., Garabedian, S.P.: Use of colloid filtration theory in modeling movement of bacteria through a contaminated sandy aquifer. Environ. Sci. Technol. **25**(1), 178–185 (1991). https://doi.org/10.1021/es00013a021

Hertz, H.: Ueber die berührung fester elastischer körper. J. für die reine und angewandte Mathematik (Crelles Journal) (1882). https://doi.org/10.1515/crll.1882.92.156

Herzig, J., Leclerc, D., Goff, P.L.: Flow of suspensions through porous media-application to deep filtration. J. Ind. Eng. Chem. **62**(5), 8–35 (1970). https://doi.org/10.1021/ie50725a003

Hogg, R., Healy, T.W., Fuerstenau, D.W.: Mutual coagulation of colloidal dispersions. Trans. Faraday Soc. **62**, 1638–1651 (1966). https://doi.org/10.1039/TF9666201638

Huang, F., Kang, Y., You, L., Li, X., You, Z.: Massive fines detachment induced by moving gas-water interfaces during early stage two-phase flow in coalbed methane reservoirs. Fuel **222**, 193–206 (2018). https://doi.org/10.1016/j.fuel.2018.02.142

Huysmans, M., Dassargues, A.: Review of the use of Péclet numbers to determine the relative importance of advection and diffusion in low permeability environments. Hydrogeol. J. **13**, 895–904 (2005). https://doi.org/10.1007/s10040-004-0387-4

Iliuta, I., Larachi, F.: Deposition and aggregation of Brownian particles in trickle-bed reactors. AICHE J. **52**(12), 4167–4180 (2006). https://doi.org/10.1002/aic.11023

Israelachvili, J.N.: Intermolecular and Surface Forces, 3rd ed. edn., Burlington, MA (2011). https://doi.org/10.1016/C2009-0-21560-1

Katz, A., Thompson, A.: Prediction of rock electrical conductivity from mercury injection measurements. J. Geophys. Res. Solid Earth **92**(B1), 599–607 (1987). https://doi.org/10.1029/JB092iB01p00599

Ke, P.C., Gu, M.: Characterization of trapping force in the presence of spherical aberration. J. Mod. Opt. **45**(10), 2159–2168 (1998). https://doi.org/10.1080/09500349808231752

Kermani, M.S., Jafari, S., Rahnama, M., Raoof, A.: Direct pore scale numerical simulation of colloid transport and retention. Part I: fluid flow velocity, colloid size, and pore structure effects. Adv. Water Resour. **144**, 103694 (2020). https://doi.org/10.1016/j.advwatres.2020.103694

Kloss, C., Goniva, C., Hager, A., Amberger, S., Pirker, S.: Models, algorithms and validation for open-source DEM and CFD-DEM. Prog. Comput. Fluid Dyn. **12**(2–3), 140–152 (2012). https://doi.org/10.1504/PCFD.2012.047457

Kretzschmar, R.: Colloid-facilitated sorption and transport. Encyclopedia of soils in the environment, pp. 276–284 (2005). https://doi.org/10.1016/B0-12-348530-4/00201-0

Kruggel-Emden, H., Wirtz, S., Simsek, E., Scherer, V.: Modeling of granular flow and combined heat transfer in hoppers by the discrete element method (DEM). J. Press. Vessel Technol. (2006). https://doi.org/10.1115/1.2218349

Li, X., Zhang, P., Lin, C., Johnson, W.P.: Role of hydrodynamic drag on microsphere deposition and re-entrainment in porous media under unfavorable conditions. Environ. Sci. Technol. **39**(11), 4012–4020 (2005). https://doi.org/10.1021/es048814t

Li, Y., Xu, Y., Thornton, C.: A comparison of discrete element simulations and experiments for 'sandpiles' composed of spherical particles. Powder Technol. **160**(3), 219–228 (2005). https://doi.org/10.1016/j.powtec.2005.09.002

Liu, S., Shikhov, I., Cui, Y., Arns, C.H.: Pore-scale morphology effects on colloid deposition by trajectory tracking simulations. Geoenergy Sci. Eng. **227**, 211772 (2023)

Lohaus, J., Perez, Y.M., Wessling, M.: What are the microscopic events of colloidal membrane fouling? J. Membr. Sci. **553**, 90–98 (2018). https://doi.org/10.1016/j.memsci.2018.02.023

Lun, C., Savage, S.B., Jeffrey, D., Chepurniy, N.: Kinetic theories for granular flow: inelastic particles in couette flow and slightly inelastic particles in a general flowfield. J. Fluid Mech. **140**, 223–256 (1984). https://doi.org/10.1017/S0022112084000586

Martys, N.S., Hagedorn, J.G.: Multiscale modeling of fluid transport in heterogeneous materials using discrete Boltzmann methods. Mater. Struct. **35**(10), 650–658 (2002). https://doi.org/10.1007/BF02480358

Meagher, D.: Octree encoding: a new technique for the representation, manipulation and display of arbitrary 3-D objects by computer (1980)

Messina, F., Tosco, T., Sethi, R.: On the failure of upscaling the single-collector efficiency to the transport of colloids in an array of collectors. Water Resour. Res. **52**(7), 5492–5505 (2016)

Mirabolghasemi, M., Prodanović, M., DiCarlo, D., Ji, H.: Prediction of empirical properties using direct pore-scale simulation of straining through 3D microtomography images of porous media. J. Hydrol. **529**, 768–778 (2015). https://doi.org/10.1016/j.jhydrol.2015.08.016

Mondal, S., Wu, C.-H., Sharma, M.M.: Coupled CFD-DEM simulation of hydrodynamic bridging at constrictions. Int. J. Multiph. Flow **84**, 245–263 (2016). https://doi.org/10.1016/j.ijmultiphaseflow.2016.05.001

Nelson, K.E., Ginn, T.R.: New collector efficiency equation for colloid filtration in both natural and engineered flow conditions. Water Resour. Res. (2011). https://doi.org/10.1029/2010WR009587

Nguyen, G.T., Chan, E.L., Tsuji, T., Tanaka, T., Washino, K.: Resolved CFD-DEM coupling simulation using volume Penalisation method. Adv. Powder Technol. **32**(1), 225–236 (2021). https://doi.org/10.1016/j.apt.2020.12.004

Popinet, S.: Gerris: a tree-based adaptive solver for the incompressible Euler equations in complex geometries. J. Comput. Phys. **190**(2), 572–600 (2003). https://doi.org/10.1016/S0021-9991(03)00298-5

Ramachandran, V., Fogler, H.S.: Plugging by hydrodynamic bridging during flow of stable colloidal particles within cylindrical pores. J. Fluid Mech. **385**, 129–156 (1999). https://doi.org/10.1017/S0022112098004121

Ramachandran, V., Venkatesan, R., Tryggvason, G., Fogler, H.S.: Low Reynolds number interactions between colloidal particles near the entrance to a cylindrical pore. J. Colloid Interface Sci. **229**(2), 311–322 (2000). https://doi.org/10.1006/jcis.2000.6986

Ravikumar, Scott, K.: Freestanding sulfonated graphene oxide paper: a new polymer electrolyte for polymer electrolyte fuel cells. Chem. Commun **48**(45), 5584–5586 (2012). https://doi.org/10.1039/C2CC31771K

Roozbahani, M.M., Graham-Brady, L., Frost, J.D.: Mechanical trapping of fine particles in a medium of mono-sized randomly packed spheres. Int. J. Numer. Anal. Methods Geomech. **38**(17), 1776–1791 (2014). https://doi.org/10.1002/nag.2276

Ruckenstein, E., Prieve, D.C.: Adsorption and desorption of particles and their chromatographic separation. AIChE J. **22**(2), 276–283 (1976). https://doi.org/10.1002/aic.690220209

Safran, S.A.: Statistical Thermodynamics of Surfaces, Interfaces, and Membranes, (2003). https://doi.org/10.1201/9780429497131

Shikhov, I., d'Eurydice, M.N., Arns, J.-Y., Arns, C.H.: An experimental and numerical study of relative permeability estimates using spatially resolved T_1-z NMR. Transp. Porous Media **118**(2), 225–250 (2017). https://doi.org/10.1007/s11242-017-0855-7

Shirgaonkar, A.A., MacIver, M.A., Patankar, N.A.: A new mathematical formulation and fast algorithm for fully resolved simulation of self-propulsion. J. Comput. Phys. **228**(7), 2366–2390 (2009). https://doi.org/10.1016/j.jcp.2008.12.006

Sokama-Neuyam, Y.A., Ginting, P.U.R., Timilsina, B., Ursin, J.R.: The impact of fines mobilization on CO2 injectivity: an experimental study. Int. J. Greenh. Gas Control. **65**, 195–202 (2017). https://doi.org/10.1016/j.ijggc.2017.08.019

Tang, K., Li, Z., Da Wang, Y., McClure, J., Su, H., Mostaghimi, P., Armstrong, R.T.: A pore-scale model for electrokinetic in situ recovery of copper: the influence of mineral occurrence, zeta potential, and electric potential. Transp. Porous Media **150**(3), 601–626 (2023)

Tsuji, Y., Kawaguchi, T., Tanaka, T.: Discrete particle simulation of two-dimensional fluidized bed. Powder Technol. **77**(1), 79–87 (1993). https://doi.org/10.1016/0032-5910(93)85010-7

Tufenkji, N., Elimelech, M.: Breakdown of colloid filtration theory: role of the secondary energy minimum and surface charge heterogeneities. Langmuir **21**(3), 841–852 (2005). https://doi.org/10.1021/la048102g

Verwey, E.J.W., Overbeek, J.T.G.: Theory of the stability of lyophobic colloids. J. Colloid Sci. **10**(2), 224–225 (1955). https://doi.org/10.1021/j150453a001

Weller, H.G., Tabor, G., Jasak, H., Fureby, C.: A tensorial approach to computational continuum mechanics using object-oriented techniques. Comput. Phys. **12**(6), 620–631 (1998). https://doi.org/10.1063/1.168744

Xiong, Q., Li, B., Zhou, G., Fang, X., Xu, J., Wang, J., He, X., Wang, X., Wang, L., Ge, W.: Large-scale DNS of gas-solid flows on Mole-8.5. Chem. Eng. Sci. **71**, 422–430 (2012). https://doi.org/10.1016/j.ces.2011.10.059

Yao, K.-M., Habibian, M.T., O'Melia, C.R.: Water and waste water filtration. Concepts and applications. Environ. Sci. Technol. **5**(11), 1105–1112 (1971). https://doi.org/10.1021/es60058a005

Zhang, M., Prodanovic, M.: Optimizing proppant placement in rough-walled rock fractures. In: Unconventional Resources Technology Conference, Denver, Colorado, 22-24 July 2019, pp. 3971–3991 (2019)

Zhou, Z., Kuang, S., Chu, K., Yu, A.: Discrete particle simulation of particle-fluid flow: model formulations and their applicability. J. Fluid Mech. **661**, 482–510 (2010). https://doi.org/10.1017/S002211201000306X